

ARTICLE OPEN



Corrosion interactions between stainless steel and lead vanado-iodoapatite nuclear waste form part I

Xiaolei Guo^{1,4}✉, Yachun Wang^{2,4}, Tiankai Yao^{2,3}, Chandi Mohanty¹, Jie Lian² and Gerald S. Frankel¹

This study explores the corrosion interactions between a metallic canister material, stainless steel (SS) 316, and an I-bearing ceramic waste form, lead vanado-iodoapatite (I-APT, $\text{Pb}_{9.85}(\text{VO}_4)_6\text{I}_{1.7}$), in a chloride solution. Crevice corrosion of the SS in close proximity to the I-APT resulted in the development of an aggressive environment at the interface of the two materials, which was acidic and enriched in Cl^- anions. I-APT also corroded in the crevice region, primarily through ion-exchange between the I^- ions from the I-APT matrix and anions from the environment. The enrichment of Cl^- anions within the occluded crevice space as the result of SS crevice corrosion enhanced the corrosion of I-APT. The release of iodine from this apatite waste form could be accelerated owing to this mechanism. This is evidenced by a depletion of iodine from the I-APT matrix and a large amount of Cl-bearing precipitates on the surfaces of both SS and I-APT. On the other hand, the corrosion of I-APT leads to the precipitation of a V- and Pb-rich layer, which inhibits the localized corrosion of SS to an extent. This study advances the understanding of the near-field corrosion interactions between metallic canisters and ceramic waste forms.

npj Materials Degradation (2020)4:13; <https://doi.org/10.1038/s41529-020-0117-y>

INTRODUCTION

The immobilization of iodine-129, one of the problematic fission products, has been a major challenge for high level waste (HLW) disposal because of its high toxicity and volatility, as well as its extremely long half-life¹. Unlike the majority of HLW, iodine mainly evolves as gas during reprocessing and cannot be properly incorporated into borosilicate glasses, which is the eventual fate of most of the HLW. Therefore, numerous waste forms have been proposed to properly confine iodine^{2–4}. Among the most promising materials developed so far, synthetic apatites, a group of ceramic waste forms inspired by natural analog apatites, have shown promise owing to their high thermal and chemical stability and radiation resistance^{5–7}.

Regardless of the waste form, the ultimate goal is to dispose of these I-129 incorporated materials underground in deep geological repositories and isolate them from human activities for tens or hundreds of thousands of years. However, it is still unclear at this moment how these ceramic waste forms will be stored in the repository. Borosilicate waste glass is being cast in metallic canisters made out of stainless steel (SS)⁸. Therefore, it is likely that any ceramic waste forms will also end up in metallic canisters, although additional materials might be added to fill the voids between them. As a result, interfaces will exist between the metallic canisters and ceramic waste forms/filling materials. Since the nature of the filling materials is not clearly defined at this point, this study only considers the interface between the canister and ceramics. We have recently reported the potential corrosion interactions between SS and other waste forms in a corrosive environment^{9,10}. Synergistic interactions were found between the SS crevice corrosion and the corrosion of Cr-bearing hollandite ceramic waste forms. The corrosion of both materials released cations such as Cr^{3+} that could accumulate within the confined crevice space between the SS and hollandite. Hydrolysis of these cations created an acidic environment, which enhanced the

corrosion of both materials. This synergistic corrosion mechanism could potentially accelerate the release of radionuclides into the environment. Therefore, when designing new waste forms, their potential corrosion interactions with metallic canisters should be considered. However, such interactions have not been reported in the literature.

In this study, the corrosion interactions between SS 316 and lead vanado-iodoapatite (I-APT, $\text{Pb}_{9.85}(\text{VO}_4)_6\text{I}_{1.7}$), a potential I-129 waste form^{5–7}, are explored. The corrosion mechanism of I-APT has been reported in previous studies^{5,11}. In general, when I-APT is exposed to an aqueous environment, the I^- ions within the I-APT matrix will exchange with other anions (e.g., OH^-) in the leaching solutions. The release rate of I^- ions via this mechanism was found to be greater than that of the uniform dissolution rate of the I-APT matrix. In solutions with neutral pH and low ionic strength, a typical environment for underground water^{12,13}, the release rate of I^- is on the order of $10^{-3} \text{ g m}^{-2} \text{ d}^{-1}$, which is quite low. However, due to the influence of metal crevice corrosion, this rate could be enhanced. As has been well documented, metal crevice corrosion not only creates metal cations from dissolution and protons from hydrolysis of those cations, but also causes the migration of aggressive anions such as Cl^- from the bulk solution to the confined crevice space to balance the charge from metal dissolution^{14,15}. Therefore, when SS is corroded in close proximity to I-APT, apart from the enhanced local acidity, the enrichment of Cl^- at the material interface could also accelerate the release of I^- ions from I-APT. With this hypothesis, the two materials were pressed against each other and corroded in 0.6 M NaCl solutions at 90 °C for a period of 28 days. Their corrosion interactions were systematically studied. The first part of the work, reported here, focuses on the crevice corrosion of SS, which provides the dominant driving force for the enhanced corrosion of the nearby I-APT. The corrosion of SS was clearly influenced by the corrosion products of I-APT. The enhanced corrosion on I-APT due to SS

¹Department of Materials Science and Engineering, Ohio State University, Columbus, OH 43210, USA. ²Department of Mechanical Aerospace and Nuclear Engineering, Rensselaer Polytechnic Institute, Troy, NY 12180, USA. ³Materials and Fuel Complex, Idaho National Laboratory, Idaho Falls, ID 83402, USA. ⁴These authors contributed equally: Xiaolei Guo, Yachun Wang. ✉email: guo.237@buckeyemail.osu.edu

crevice corrosion is characterized in Part II of this study. A new synergistic corrosion mechanism is proposed for near-field corrosion interactions, which could influence the integrity of nuclear waste packages. Since the immobilization of I-129 is a global issue, the present study is relevant to the nuclear waste disposal worldwide. However, the oxic environment used in this work reflects the conditions for the U.S. Yucca Mountain project¹⁶, while anoxic disposal conditions in the saturated zone have been proposed by many other countries¹⁷. More discussions on the implications of this study to anoxic environments are provided in Part II.

RESULTS

Corrosion morphology of SS

To simulate the near field corrosion interactions between SS metallic canisters and encapsulated ceramic nuclear waste forms, SS was corroded in close proximity to I-APT in 0.6 M NaCl solution at 90 °C. In the actual disposal relevant environment, the initial Cl⁻ concentration will likely be much lower^{12,13}. However, the Cl⁻ ions could be enriched due to localized corrosion¹⁴, so 0.6 M NaCl solution is a reasonable surrogate for a repository environment⁹. The corrosion morphology of the corroded SS is shown in Fig. 1. Crevice corrosion was found on SS after only 7 days of exposure as indicated by the white arrows in the topographic map in Fig. 1a. A large amount of precipitates is visible near the boundary of the SS/I-APT contact area (hereafter referred to as crevice mouth area). As shown in the optical photographs in Fig. 1b, c, these precipitates were observed primarily within the crevice, as clearly delineated by a dark band showing the boundary of the SS and I-APT contact area. The magnified 3D topography image in Fig. 1d shows that the crevice was about 10–20 μm wide and 1 μm deep. Note that the unidirectional scratches present on the sample surface were caused by surface abrasion during the sample preparation. Similar scratches were also present on the pristine SS as shown in Fig. 1e. After 28 days of exposure, the contrast between the areas inside and outside the crevice became more evident (Fig. 1f). The precipitates also became larger in diameter, suggesting the growth and aggregation of such phases over time, but they were still located within the crevice. The 3D topography image suggests that the width of the crevice became larger compared to that at 7 days, but the depth remained essentially unchanged (Fig. 1g). The corrosion damage observed near the crevice mouth is a typical characteristic of crevice corrosion, which could be attributed to the low ohmic potential drop from the exterior cathode relative to the interior¹⁵. SS was also corroded in close proximity to polytetrafluoroethylene (PTFE), which is assumed to be inert. In comparison to the I-APT case, the SS shows a higher degree of corrosion in a crevice with PTFE, as indicated by the large amount of corrosion products precipitated in the crevice mouth region and the deeper crevice damage (~3 μm) shown in Fig. 1h. In addition, multiple large pits with diameter over 100 μm were also identified within the crevice (Fig. 1i). Comparing the SS corroded in close proximity to I-APT and PTFE, it is clear that the extent of crevice corrosion of SS in contact with I-APT was less than that in contact with PTFE, suggesting that the SS attack was suppressed by the corrosion products of I-APT.

The corrosion morphology of SS corroded with I-APT was also studied by SEM. As shown in Fig. 2a, b, no large pits or deep crevice regions are visible for areas inside or outside of the crevice. However, the entire surface was covered by numerous precipitated particles on the nanometer scale. The precipitates shown in Fig. 1f were also examined by SEM, which indicated that the precipitates were formed by aggregation of a large amount of smaller particles (Fig. 2c). EDS elemental maps (Fig. 2d) suggest that these precipitates were enriched in Pb and V, which were the corrosion products of I-APT. However, no iodine was observed.

This may be associated with the precipitation of Cl-rich apatites during the corrosion of I-APT, as supported by the strong Cl signal in the EDS elemental map. Studies have shown that Pb₅(VO₄)₃Cl is the primary corrosion product of I-APT in NaCl solutions¹¹. The precipitation of I-rich apatite is less favorable in solutions containing Cl⁻ ions due to the ion-exchange corrosion mechanism. The absence of iodine in these precipitates is in accordance with observations described in Part II of this study. In addition, no Fe, Cr, or Ni was identified in the precipitates. However, Mo appears to be enriched, indicating the incorporation of corroded SS elements in the precipitated phases.

Raman spectroscopy

The corroded SS surface was also examined by Raman spectroscopy, and the results are shown in Fig. 3. Measurements were only conducted in the area within the crevice, where precipitates were visible by optical microscopy. Spectra were acquired from the precipitated phases (indicated as Spots 1–3 in Fig. 3) and also from the SS surface between visible precipitates (indicated as Matrix in Fig. 3). A number of peaks were identified, most of which are in accordance with those observed on I-APT corroded in bulk solutions¹⁸. For example, the peak at 247 cm⁻¹ was due to the translational and rotational vibrations of tetrahedral VO₄³⁻, while the 316 cm⁻¹ band was attributed to the bending vibrations of VO₄³⁻¹⁸. The strong peak at 826 cm⁻¹ was ascribed to the stretching vibrations of VO₄³⁻¹⁸. These three peaks may be associated with Pb₅(VO₄)₃Cl, which is the corrosion product of I-APT as will be described in Part II. However, a new broad band between 900 and 1020 cm⁻¹ was observed for all four spectra, which was absent in the previous work¹⁸. This band may be associated with the formation of new vanadate species due to hydrolysis¹⁹, which were deposited on the entire SS surface as a film. These new species could be VO₂⁺, VO₂(OH)₂⁻, VO₃(OH)₂⁻, etc.²⁰, depending on the local pH values. The bands between 200–400 cm⁻¹ and 800–1020 cm⁻¹ could also be associated with molybdenum oxides²¹, which partially overlap with those of vanadate species. The broad feature of the peak made it difficult to identify with confidence. It will be shown in Part II that the broad bands between 900 and 1020 cm⁻¹ were not observed on the surface of the nearby I-APT, suggesting that the presence of SS may cause further alteration or degradation of the corrosion products of I-APT. Meanwhile, these altered corrosion products could in turn affect the corrosion of SS.

X-ray photoelectron spectroscopy (XPS)

The corroded SS was also subjected to XPS analysis to better understand its surface chemistry and thus the underlying corrosion mechanisms. Randomly selected areas inside and outside the crevice were examined, as shown in Figs. 4 and 5. The concentrations of cations in the surface layer were quantified and the results are plotted in Fig. 6. As shown in Fig. 4a, b, the Fe and Cr spectra were fitted with multiplex structures²². Fe, Cr, and Mo were identified in both areas, but the film from the area inside the crevice exhibited less metallic phases, suggesting the presence of a thicker surface layer.

The SEM/EDS (Fig. 2) results indicated that Mo was present in the corrosion products within the crevice, while Fe and Cr were absent. Therefore, Mo seems to play a role in the corrosion interactions of SS and I-APT. To better understand this role, Mo spectra collected from the surface of SS corroded in close proximity to PTFE under similar testing conditions are given in Fig. 4c. For this control experiment, the areas outside (referred to as region i) and inside the crevice (referred to as region ii) were compared. In region i, Mo exists in four different oxidation states, including metallic Mo (227.4 eV)^{23,24} from the SS substrate, MoO (228.4 eV)^{24,25}, Mo₄O₁₁ (231.3 eV)²⁶, and MoO₃ (232.6 eV)²⁷. However, only the highest oxidation state of Mo (MoO₃, 232.6 eV)²⁷

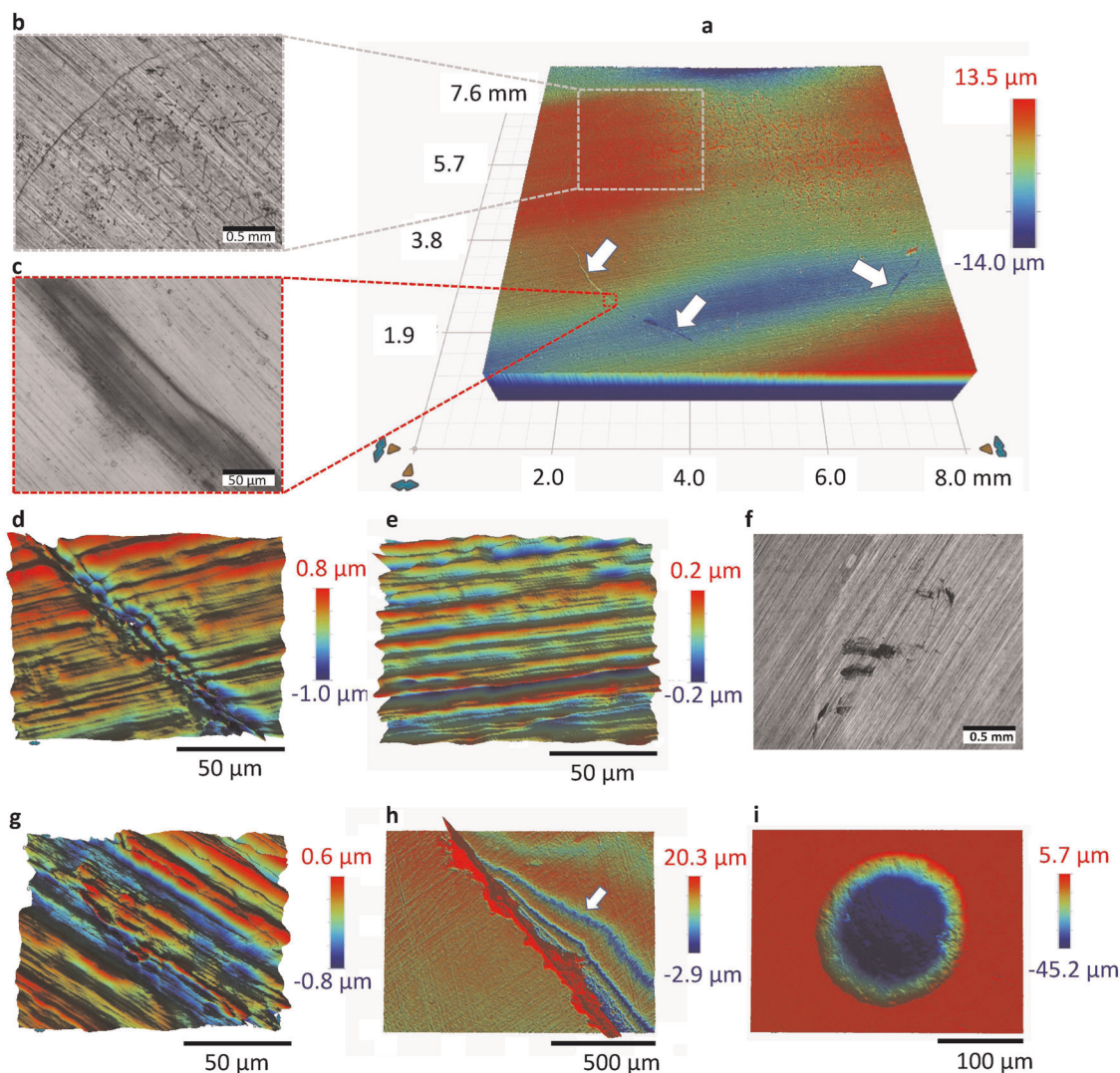


Fig. 1 Morphology of SS after corrosion in close proximity to I-APT (denoted as (SS + APT)) or PTFE (denoted as SS(+PTFE)). All photos were taken on the contact side. **a** 3D topography of SS(+I-APT) after 7 days of corrosion. **b, c** Optical microscopy images of SS(+I-APT) showing the boundary of SS/I-APT contact area after 7 days of corrosion. **d** 3D topography of the crevice damage on SS(+I-APT) after 7 days of corrosion. **e** 3D topography of a pristine SS. **f** Optical microscopy image of the SS/I-APT boundary area on SS(+I-APT) after 28 days of corrosion. **g** 3D topography of the crevice damage on SS(+I-APT) after 28 days. **h** 3D topography of the SS/PTFE boundary area on SS(+PTFE) after 28 days of corrosion. The white arrows indicate the location of crevice corrosion. **i** 3D topography of SS(+PTFE) showing a typical pit observed inside the crevice.

was observed in region ii, which is a stable form of oxide that can exist in acidic environment²⁸. This further validated the aggressive environment inside the crevice formed between SS and PTFE.

Interestingly, the oxidation states of Mo for SS corroded in close proximity to I-APT were different than the control group corroded near PTFE. For the area outside the crevice, four oxidation states were observed. The peaks centered around 227.4 and 228.4 eV were attributed to metallic Mo from the SS substrate and MoO, respectively, which are similar to those observed in region i. The third peak was centered at 229.8 eV, which corresponds to MoO₂²⁹. The fourth peak was centered at 232.2 eV, which has been ascribed a nonstoichiometric Mo^{δ+} oxide ($5 < \delta < 6$)^{24,30}. The latter two peaks were located at lower binding energies than those of Mo₄O₁₁ (231.3 eV)²⁶, and MoO₃ (232.6 eV)²⁷, which were observed in region i. This suggests that the crevice environment for SS and I-APT was less aggressive than that of SS and PTFE, which may be associated with the corrosion inhibition effect of I-APT corrosion products. For the area inside the crevice, the following oxidation states were observed: metallic Mo from the SS

substrate (227.4 eV), Mo³⁺ (228.7 eV)²⁴ probably in oxide forms, MoCl₃ (230.4 eV)³¹, and a nonstoichiometric oxide Mo^{δ+} ($5 < \delta < 6$)^{24,30}. The presence of MoCl₃ is consistent with the SEM/EDS result shown in Fig. 2d, which may be associated with the migration of Cl⁻ ions into the crevice, a typical process occurs during metal crevice corrosion^{14,15}. The enrichment of Cl⁻ ions in the confined crevice region not only enhanced the corrosion on SS by undermining the integrity of SS passivity³², it also enhanced corrosion on the nearby I-APT, which is discussed in Part II.

In addition to the elements that originated from SS, Pb, V, and Cl were also present on the surface of the corroded SS (Fig. 5). V and Pb species, the corrosion products of I-APT, were identified both inside and outside of the crevice (Fig. 5a). For the area inside the crevice, the V 2p_{3/2} peak was centered at 516.8 eV, corresponding to V⁵⁺ species (V₂O₅ or its hydrates such as VO₄³⁻)³³. It should be noted that V 2p_{1/2} partially overlaps with the O 1s peak, so fitting was only conducted on the 2p_{3/2} peak. The Pb peak at 138.5 eV could be attributed to Pb₂³⁴, Pb(OH)₂³⁵, PbCl₂,³⁶ or Pb₅(VO₄)₃Cl. However, iodine was absent on the SS

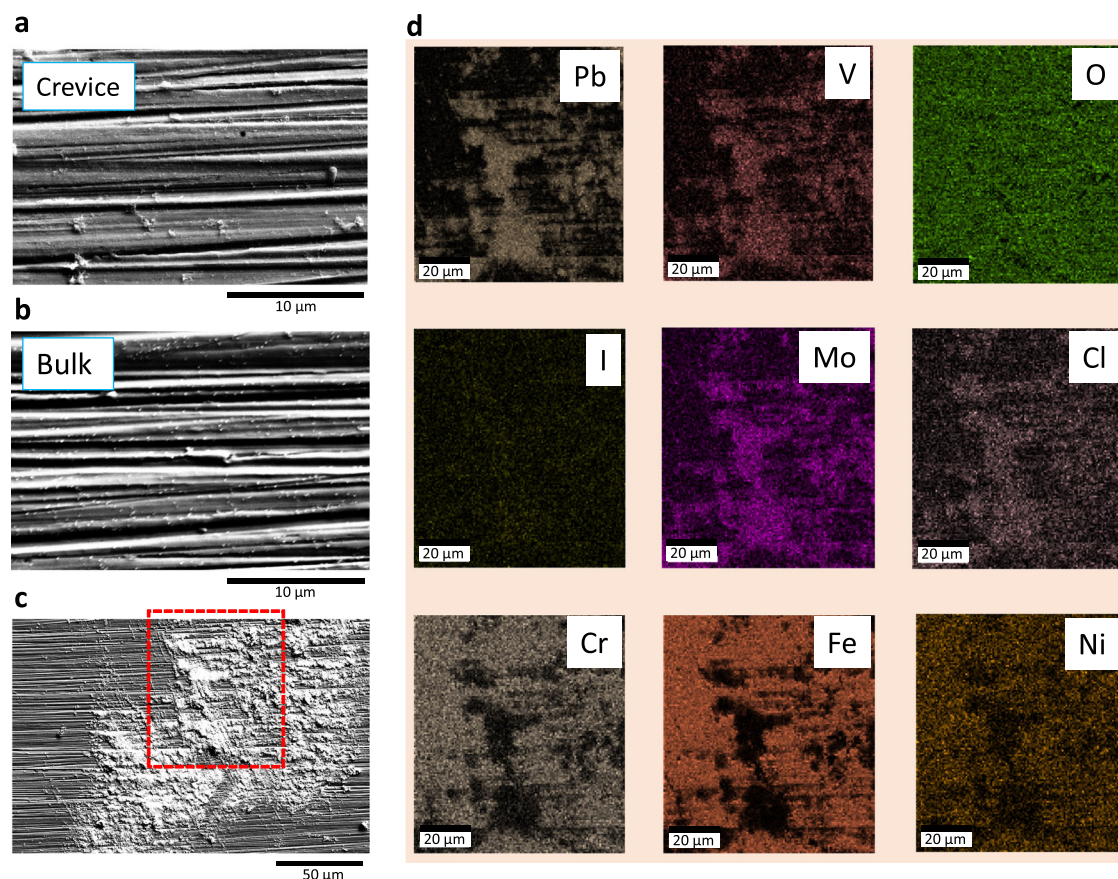


Fig. 2 SEM/EDS analysis for SS corroded in close proximity to I-APT. **a** A typical area within the center of the crevice. **b** A typical area outside crevice. **c** An area near the crevice mouth where massive precipitation was observed. The red box shows where the EDS elemental mapping was acquired. **d** EDS elemental mappings of precipitates observed near the crevice mouth.

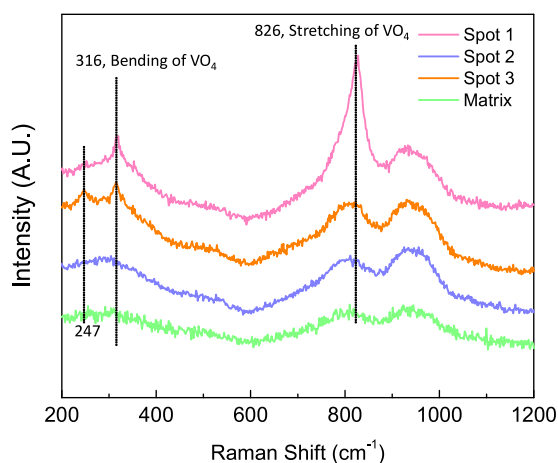


Fig. 3 Raman spectra acquired from SS corroded in close proximity to I-APT. Spectra from three different spots in the crevice as well as from the matrix are shown.

surface (Fig. 5d), so PbI_2 was ruled out. $\text{Pb}_5(\text{VO}_4)_3\text{Cl}$ is the corrosion product of I-APT, which has been observed on the surface of I-APT (see Part II). Therefore, it is likely that the Pb is present as $\text{Pb}_5(\text{VO}_4)_3\text{Cl}$. However, $\text{Pb}(\text{OH})_2$ and PbCl_2 may also exist on the SS surface, which is discussed below. Cl only exists inside the crevice, most likely as $\text{Pb}_5(\text{VO}_4)_3\text{Cl}$ due to its low solubility. These results further supported the notion that the corrosion of I-APT is primarily through the ion exchange between I^- and Cl^- ^{11,37}, since

$\text{Pb}_5(\text{VO}_4)_3\text{Cl}$ is the dominant ion-exchange product of I-APT in NaCl solutions¹¹. For the area outside the crevice, the V and Pb peaks both varied slightly (~ 0.1 eV) compared to those from the area inside the crevice. Since no I or Cl was present in the areas outside of the crevice, the observed V and Pb peaks were ascribed to $\text{Pb}_3(\text{VO}_4)_2$, rather than $\text{Pb}_5(\text{VO}_4)_3\text{Cl}$. This is expected because $\text{Pb}_3(\text{VO}_4)_2$ is a typical corrosion product for I-APT⁵. In addition, VO_4^{3-} could remain stable in alkaline solutions²⁰, the expected conditions for the area outside of crevice where oxygen reduction reaction (ORR) dominates.

The XPS quantification (Fig. 6) show that the concentration of Fe^{3+} cations in the surface layer was significantly higher for the area inside the crevice compared to outside, while the opposite was observed for Cr^{3+} . Since metallic Fe and Cr peaks were observed (originated from the metal substrate), the detection depth of XPS seems to have included the entire thickness of the passive film. Therefore, the decrease of Cr concentration inside the crevice is not a consequence of the changes in the SS passive film. Instead, it may be due to the presence of a thicker but heterogenous layer of corrosion products on top of the SS passive film. This is consistent with the SEM/EDS data shown in Fig. 2d. The concentration of Mo is very low, which is similar for the areas inside and outside the crevice. The concentration of V is also similar in both areas. However, the concentration of Pb^{2+} is one order of magnitude higher inside the crevice than the outside. Comparing the Pb/V ratio, it may be concluded that Pb and V may exist in multiple different phases. For the area outside the crevice, the Pb/V ratio is about 0.3, suggesting that they may exist as $\text{Pb}_3(\text{VO}_4)_2$ and V_2O_5 , since no Cl^- was detected in this area. For the area inside the crevice, the Pb/V ratio is about 4.5. Therefore, in

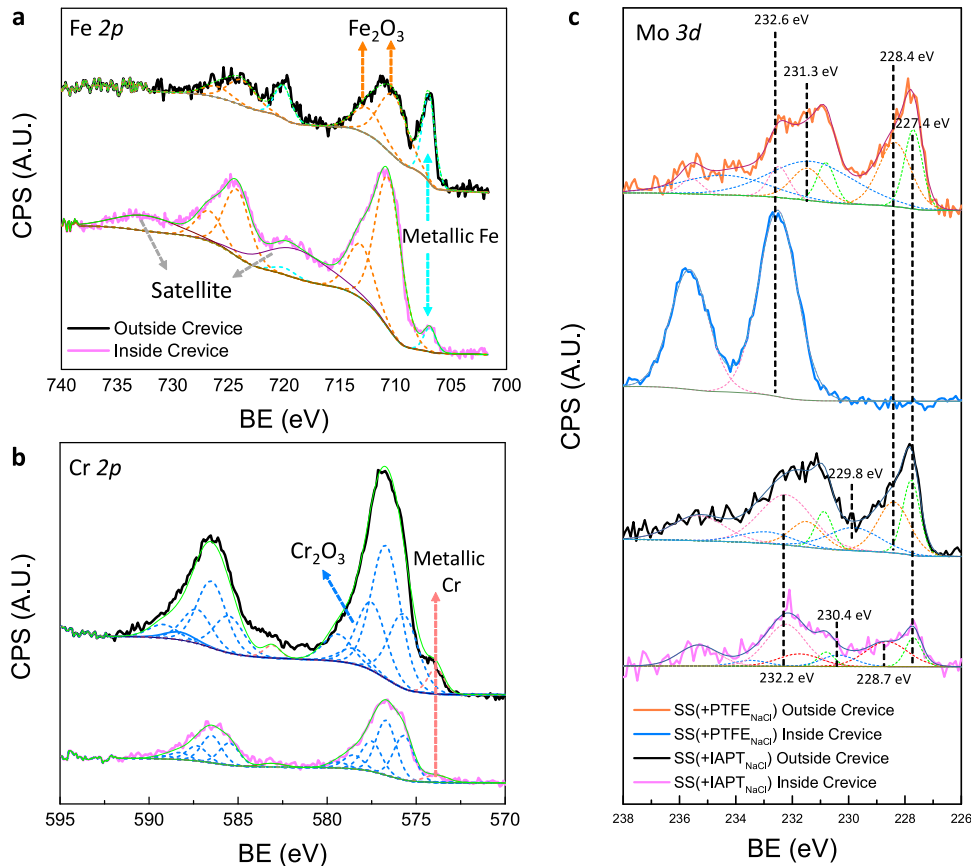


Fig. 4 XPS spectra of SS corroded in close proximity to I-APT. **a** Fe 2p, **b** Cr 2p, **c** Mo 3d. The I-APT in the legend stands for I-APT. SS (+PTFE_{NaCl}) stands for a control group of SS corroded in close proximity to PTFE in NaCl.

addition to Pb₅(VO₄)₃Cl (Pb/V of 1.7) and Pb₃(VO₄)₂ (Pb/V of 1.5), PbCl₂ is also likely present in this area, otherwise the Pb/V ratio would not exceed 1.7. Pb(OH)₂ can be ruled out due to its instability in acidic environment.

Scanning transmission electron microscopy (STEM)

To further explore the changes of structure and chemistry on the surface of the corroded SS, TEM characterization was performed. Foils from outside and inside the crevice were lifted out from the corroded SS surface by focused ion beam. As shown in Fig. 7a–c, a layer of corrosion products is visible on the corroded SS surface outside of the crevice. EDS elemental maps suggest that the precipitated particles are primarily iron oxides (Fig. 7d, d1–d4), which may be Fe₂O₃ as indicated by the XPS results in Fig. 2c. A Cr-enriched thin layer delineates the location of the SS passive film (Fig. 7d3). An EDS line scan was conducted along the black arrow in Fig. 7d. The scanning was initiated from the particle enriched in Fe₂O₃, where a noticeable amount of Pb was also present, suggesting the co-precipitation of corrosion products from SS and I-APT. When the passive film was encountered, an abrupt decrease of Pb, and O was observed, accompanied by a sharp increase of Cr and Ni. An evident depletion of Fe was also identified in the passive film. The delayed onset of the Ni signal compared to Cr suggests that Cr oxides were located on top of a Ni rich layer. When the beam reached the SS substrate, a plateau was observed for all elements including Fe, Cr, Ni, and O. The amount of O observed is likely due to the oxidation of the foil upon removal from the vacuum of the focused ion beam (FIB) tool used for liftout. No Mo was detected due to its low concentration in SS.

Similar characterization was conducted on three different locations of the foil harvested from an area inside the crevice.

The results are shown in Figs. 8–10. As indicated by the white arrows shown in Fig. 8a, b, a surface film thicker than that observed in Fig. 7 was consistently observed in the crevice. EDS elemental maps show that the film was enriched in Pb, V, Cl, and O, which are corrosion products of I-APT. An EDS line scan along the arrow in Fig. 8b indicates that this layer was approximately 100 nm in thickness (see Fig. 8d), which is about 10× higher than the detection depth of XPS (~10 nm)³⁸. The lateral sampling area for the XPS instrument was about 400 μm × 600 μm. However, as shown in Figs. 4 and 5, XPS was able to detect the metallic components of SS such as Fe and Cr. This suggests that the detected precipitated layer must have variable thickness, with thickness less than 10 nm in some locations.

A higher magnification image showing heterogeneity in the thickness of the deposited layer is shown in Fig. 9a. EDS analysis revealed four different regions (Fig. 9b, c): (i) the outermost layer enriched in Pb, V, O, and Cl, which was likely from the precipitated Pb₅(VO₄)₃Cl nanoparticles. Interestingly, there is about 5% Fe in this region, suggesting the incorporation of Fe corrosion products within this layer; (ii) a layer enriched in Fe, Pb, and O, which may be the co-precipitates of iron oxides and PbCl₂; (iii) the SS passive film, which is depleted in Fe but enriched in Cr (outer layer) and Ni (inner layer). This layer is about 4 nm thick, which is typical for a passive film; and (iv) the SS substrate where the concentration of Fe, Cr, and Ni are invariant, and the concentration of each element agrees with the nominal concentrations of SS. This structure is somewhat similar to what was observed for SS 316 corroded in pressurized water reactors environment^{39,40}, where a two-layered oxide was identified: a Cr-rich inner layer and an Fe-rich outer layer. It was suggested that the Cr-rich inner layer was formed by solid state growth while the Fe-rich outer layer was formed by metal dissolution and reprecipitation³⁹, which agrees well with the

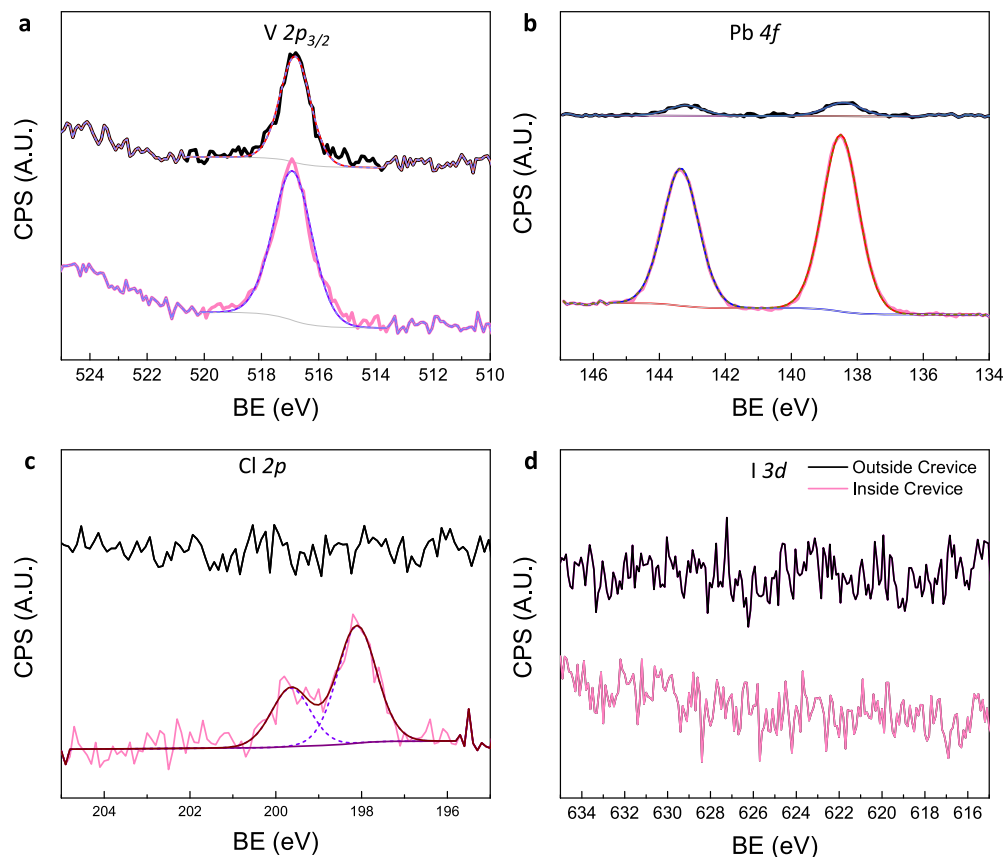


Fig. 5 XPS spectra of SS corroded in close proximity to I-APT. **a** V $2p_{3/2}$, **b** Pb 4f, **c** Cl 2p, and **d** I 3d.

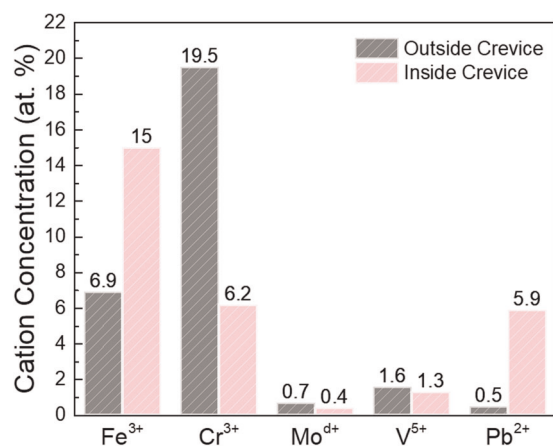


Fig. 6 Quantification of different cations present in the surface layer of SS corroded in close proximity to I-APT. The concentration calculation was based on XPS peak area and the relative sensitivity factor of the corresponding species.

observations in this study, although the environment is not completely the same. It is worth noting that no evident Fe, Cr, and Ni were detected in the precipitates as revealed by SEM/EDS (Fig. 2). Although Fe and Cr were identified in XPS analysis, the large lateral sampling area ($400\ \mu\text{m} \times 600\ \mu\text{m}$) and heterogeneous distribution of precipitates made it difficult to distinguish the source of these two elements with confidence. With STEM/EDS analysis, the distribution of these elements was clearly identified. It is evident that the altered SS passive film contained Fe, Cr, and Ni,

while only Fe was present in the precipitates. The relatively smaller amount of Fe in the precipitates seemed to have been overwhelmed by the much larger amount of Fe signal originated from the surrounding SS substrate.

Interestingly, a nano-crack was observed in a different area from the same foil (Fig. 10a), which is located beneath the deposited layer. EDS analysis suggests that the crack is depleted in Fe and Ni, while enriched in Cr and O (Fig. 10b–f, h), suggesting the oxidation of the crack flanks. The preferential dissolution of Fe and Ni compared to Cr may be explained by the high metal–oxygen bond strength and low metal–metal bond strength for Cr⁴¹. Upon exposure to a corrosive environment, the Cr–Cr bond can break easily due to its low bond strength. This is followed by the formation of Cr–O bond, which is strong enough to resist the corrosion attack. On the other hand, the weak bond strengths for Fe–Fe, Fe–O, Ni–Ni, and Ni–O make Fe and Ni more susceptible to metal dissolution and resistant to form a stable oxide layer compared to Cr. It should be noted that the oxidation of the crack flanks could lead to a volume expansion of over 200% compared to its original volume³⁹, thus inducing residual stress that could drive the crack to advance further.

DISCUSSION

The occurrence of crevice corrosion of SS was indicated by the localized damage (Fig. 1) and Cl-rich precipitates (Fig. 2) observed in the crevice mouth region. As mentioned above, the metal crevice corrosion could generate an aggressive environment that is enriched in H⁺ and Cl[−] ions, which may cause the accelerated corrosion observed on both the SS and I-APT specimens. However, due to a feedback effect of corrosion products originated from I-APT, these accelerated reactions seem to be self-limiting. As shown in Fig. 1, the amount of corrosion observed on SS corroded

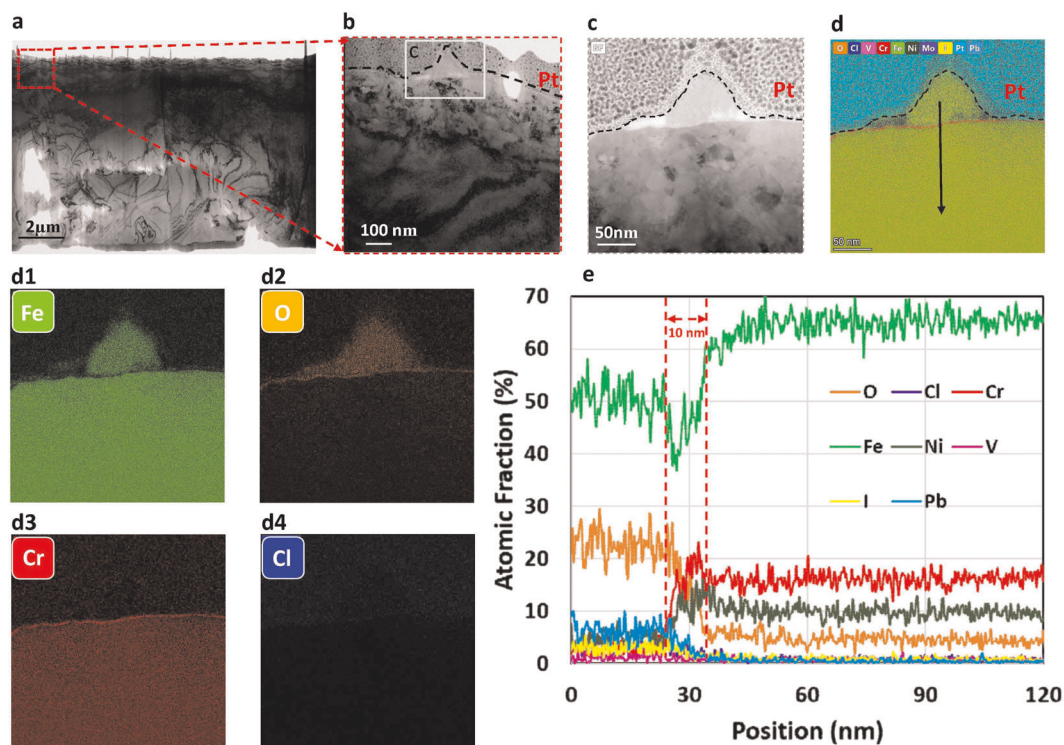


Fig. 7 STEM/EDS characterizations for the cross-section of a sample lifted from an area of SS that was located outside the crevice. **a–c** STEM images showing the existence of a surface layer on the corroded SS surface. **d** Combined EDS elemental map (O, Cl, V, Cr, Fe, Ni, Mo, I, Pb, Pt) for the area shown in (c). **d1–d4** Individual EDS elemental map for the area shown in (c). **e** EDS line scan for a region as indicated by the black arrow shown in (d).

in close proximity to I-APT is less than that of the SS corroded with PTFE. PTFE is generally believed to be an inert material due to its high chemical stability even at elevated temperature, although it can release a small amount of F^- ions into the solutions. However, the concentration of any released F^- would be much smaller than the amount of Cl^- ions in the leaching solution (0.6 M), so F^- ions were unlikely to play a significant role under the testing conditions. This suggests that the corrosion of I-APT released species that inhibited the corrosion of SS. Owing to the simple chemical composition of I-APT, it is reasonable to speculate that the inhibition effect primarily came from ions of V and/or Pb. These species were dissolved from the I-APT matrix, and precipitated from the solution onto the SS surface, leading to the observed surface layers shown in Figs. 7–10. However, the presence of SS seemed to cause further alteration of the corrosion products of I-APT, as evidenced by the presence of new Raman peaks observed in Fig. 3, and new species identified in XPS. Combining the results of XPS and STEM/EDS, it may also be concluded that the precipitated layer is not homogeneous, and the local thickness is less than 10 nm. Despite the heterogeneity of the film, its corrosion inhibition effect on SS was evident. However, this layer failed to completely eliminate the localized corrosion on SS, since localized damage was still observed. It is also possible that the localized corrosion occurred initially but was suppressed after the establishment of the Pb/V-rich surface layer. Long-term corrosion testing is required to further understand this phenomenon. Nonetheless, the possible inhibition mechanisms of ions of V and Pb are discussed in the following section.

The corrosion inhibition effect of vanadate species has been well documented for aluminum alloys^{42–45}. In general, vanadate forms an insoluble oxide layer on the surface of aluminum alloys over a wide range of pH. This layer not only blocks the anodic reactions on reactive sites, but also suppresses the ORR kinetics⁴². Adsorption of the vanadate species can also compete with the

adsorption of Cl^- ions from solution, and thus reduce the breakdown of the active intermetallic particles that are more vulnerable to localized corrosion in Al alloys. However, the inhibition efficiency of vanadate strongly depends on its speciation in the particular environment. Metavanadate ions formed in alkaline environment are excellent inhibitors, but the inhibition effect of decavanadate ions that are predominant in acidic environment is poor⁴². This may partially explain the more severe corrosion observed inside the crevice, where acidic environment existed. However, it was difficult to distinguish different hydrated species on the surface via XPS due to the low concentration.

Compared to aluminum alloys, few studies on the inhibition effect of vanadate on SS have been reported. Anderko et al. showed that metavanadate could suppress the localized corrosion of SS 316L in solutions containing Cl^- ions at both room temperature (23 °C) and an elevated temperature of 60 °C.⁴⁶ The authors suggested that the optimum inhibition efficiency was achieved at concentrations in the range of 0.1–1 M. That study was focused on developing a quantitative model to predict the repassivation potential for localized corrosion, so no detailed corrosion mechanism was discussed.

Vanadate has been investigated as a corrosion inhibitor on carbon steels. Morks et al.⁴⁷ found that Na_3VO_4 works as a good anodic corrosion inhibitor on carbon steels in both acidic and alkaline environments. Cathodic inhibition was not observed in that study. After exposure in acidic environment, a V_2O_5 film was established on the surface of the corroded carbon steel. Interestingly, the optimum inhibition efficiency was achieved at a low concentration (0.027 mM in alkaline solution and 1 mM in acidic environment). Sribharathy et al.⁴⁸ found that metavanadate ions could inhibit the corrosion of carbon steel in neutral solutions containing ~ 1.7 mM Cl^- ions. The weight loss study showed that the inhibition efficiency of vanadate increased with concentration (up to 2 mM). The authors suggested that the surface was covered

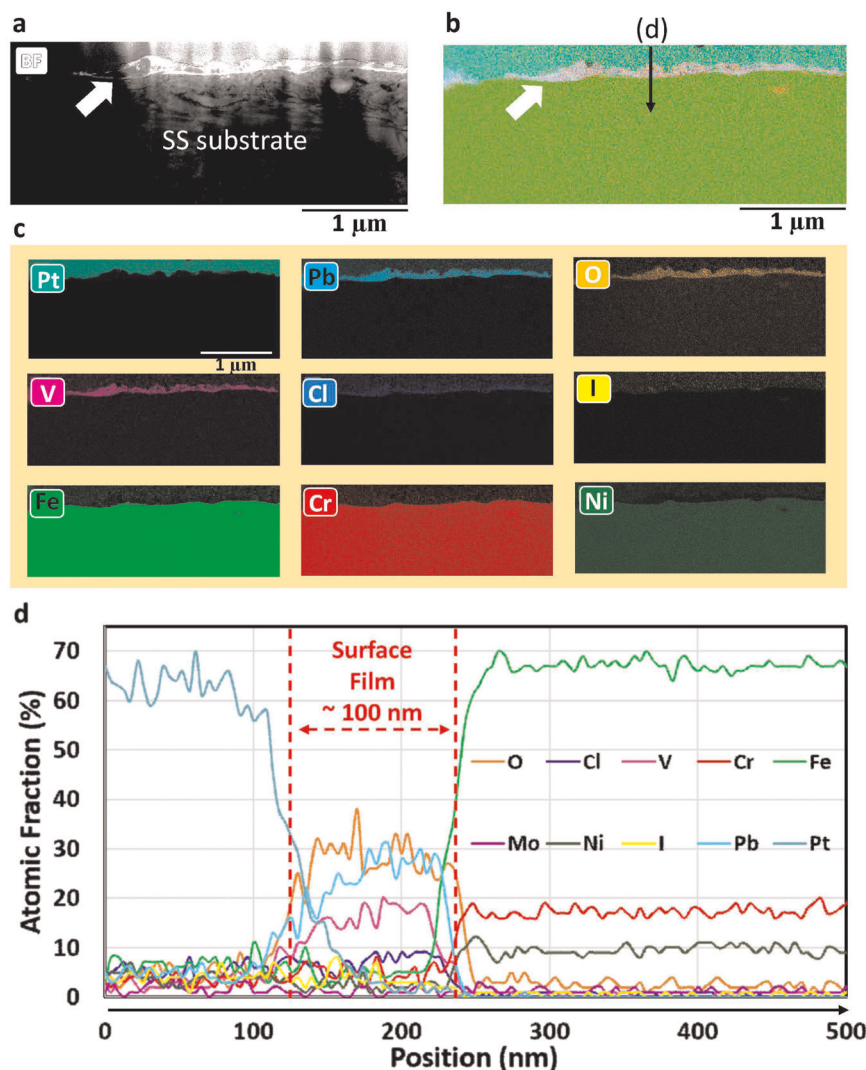


Fig. 8 STEM/EDS characterizations for the cross-section of a sample lifted from an area of SS that was located inside the crevice. **a** A bright-field STEM image showing the presence of a surface film on the corroded SS surface. **b** Combined EDS elemental map (O, Cl, V, Cr, Fe, Ni, Mo, I, Pb, Pt) for the area shown in **(a)**. **c** Individual EDS elemental map for the area shown in **(c)**. **d** EDS line scan for a region as indicated by the black arrow shown in **(b)**.

by $\text{Fe}(\text{VO}_3)_2$ but no direct evidence was provided. Zou et al.⁴⁹ developed vanadium conversion coatings on electrogalvanized steel substrates, which conferred a substantial reduction of both anodic and cathodic kinetics. The enhanced corrosion resistance was ascribed to the formation of closely packed particles on the steel surface, consisting of V_2O_5 , VO_2 oxides and the corresponding hydrates. A similar conversion coating based on vanadyl oxalate (VOC_2O_4) was developed by Gao et al.⁵⁰. After the conversion process, a vanadate oxide layer was formed on the hot-dip galvanized steel substrate, which provided cathodic inhibition to the substrate. Prior to the corrosion exposure, XPS revealed that the major V $2p_{3/2}$ peak was centered at 516.5 eV, which is very close to what was observed in this study (516.8 eV). However, the peak was ascribed to V^{4+} instead of V^{5+} . After salt spray exposure for 72 h, the V^{4+} was completely transformed into V^{3+} , which was not observed for the corroded samples in this study. The differences may be due to the presence of the galvanized layer on top of their steel substrate, which might have caused the reduction of V^{4+} during corrosion.

Similar to vanadate, limited literature exists for the effect of Pb^{2+} cations on the corrosion of steels. Shropshire reported that heavy metal ions such as Pb^{2+} could inhibit the corrosion of

1010 steels under acidic conditions due to the formation of an insoluble PbS layer on the steel surface⁵¹. The concentration of S is typically present as an impurity in 1010 steel in the range of 0.02–0.05 wt%. For SS 316, the concentration of S is typically less than 0.03 wt%, which is in the same range. However, unlike carbon steels that corrode uniformly in acidic environment, the SS specimens primarily corrode through localized corrosion such as pitting or crevice corrosion under the testing conditions. The corrosion morphologies observed in Fig. 1 also validated that the active dissolution of SS was limited to some small areas (crevice mouth region). Therefore, the amount of S released into the solution is likely limited, which may not be sufficient to form a protective Pb sulfide layer. In addition, S was not detected by XPS, which also ruled out the possibility of PbS formation.

Mayne et al. reported that Pb^{2+} could reduce the corrosion of mild steels in the pH range 4.5–7.0⁵², which was ascribed to the deposition of a lead-rich surface layer. In that study, the steel specimens were corroded in water baths containing radioactive ^{210}Pb cations, which enabled the direct observation of the Pb distribution on the steel surface via autoradiography. The authors indicated that metallic Pb was formed on top of the steel substrate, which seems unlikely even though the potential was

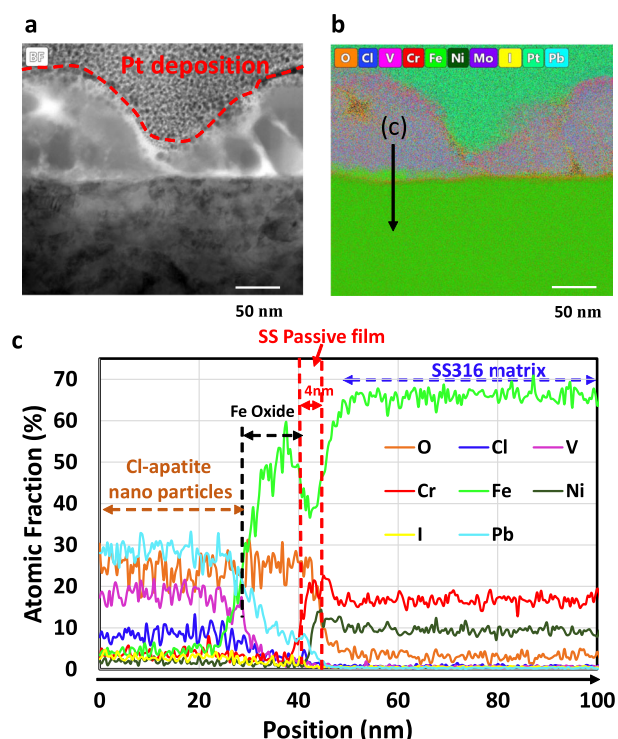


Fig. 9 STEM/EDS characterizations for the cross-section of a sample lifted from an area of SS that was located inside the crevice. **a** A bright-field STEM image showing the presence of precipitates on the corroded SS surface. **b** Combined EDS elemental map (O, Cl, V, Cr, Fe, Ni, Mo, I, Pb, and Pt) for the area shown in (a). **c** EDS line scan for a region as indicated by the black arrow shown in (b).

sufficiently low on the steel surface (~ -488 mV_{SCE}). The deposition of metallic Pb may partially block the anodic sites from dissolution, but it did not form a compact and robust film that could lead to reduced corrosion on the steel. Incomplete surface coverage of metallic Pb could not have resulted in the observed decrease in the corrosion rate since sufficient anodic sites were still available. Instead, the conductive Pb film could cause galvanic interactions between the film and steel substrates, which could increase the corrosion rate of the steel. Unfortunately, no surface analysis was performed on the corroded samples, so the chemistry of the deposited layer is unknown. However, the reduced corrosion rate could be better explained by the deposition of Pb(OH)₂ layers, rather than metallic Pb, since Pb(OH)₂ is more effective as a physical barrier against corrosion owing to its low solubility and electron conductivity.

Lafranconi et al.⁵³ reported that Pb²⁺, present even in trace amounts, could inhibit the stress corrosion cracking of SS 304 in acidic chloride media. The inhibition mechanism is associated with the underpotential deposition of Pb²⁺, which suppresses the adsorption of hydrogen atoms on the SS surface and thus reduces the cathodic kinetics. In their work, the dominant cathodic reaction is the hydrogen evolution reaction (HER), so the presence of Pb²⁺ had a significant effect. The dominant cathodic reaction in this study is ORR. However, HER could also be evoked especially within the crevice, owing to the low local pH and potential⁵⁴. Therefore, in this study, Pb²⁺ may have also played a similar role by suppressing the HER that could occur within the crevice. However, it is also possible that Pb²⁺ could be an inhibitor of the ORR, which needs further investigation.

To summarize, it may be concluded that V and Pb species inhibited the corrosion of SS exposed in close proximity to I-APT, either by the formation of an insoluble surface layer or as solution

inhibitors. Results obtained in this study are more in favor of the formation of an insoluble surface layer.

In this Part I of two papers, the corrosion in chloride solution of SS pressed against I-APT was systematically studied. Crevice corrosion was observed in the crevice mouth region after only 7 days of exposure. The crevice damage became wider but remained shallow in depth after 28 days. The corrosion was more severe on the SS corroded in close proximity to PTFE than near I-APT, suggesting an inhibitive effect of I-APT corrosion products. Surface analysis indicated that the corrosion products of I-APT and SS co-precipitated on the surface of SS passive film. In general, the precipitated layer consists of an outer layer enriched in Pb and V and an inner layer enriched in Fe. The Pb- and V-rich layer may be responsible for the reduced corrosion damage observed on the SS corroded in close proximity to I-APT. Although the corrosion of SS was suppressed by the corrosion products of I-APT, the aggressive environment created by SS crevice corrosion still has a significant effect on I-APT, the details of which are discussed in Part II.

METHODS

Materials

SS 316 sheet (UNS S31600, Cr 16–18%, Ni 10–14%, Mo 2–3%, Mn <2%, Si < 0.75%, C < 0.08, P < 0.045, S < 0.03, Fe balance, all in weight percent) was purchased from McMaster-Carr. The sheet was cut into 2.5 cm × 2.5 cm × 0.3 cm specimens and abraded to 1200 grit with SiC papers for the corrosion experiments. The I-APT (Pb_{9.85}(VO₄)₆I_{1.7}) was synthesized via a spark plasma sintering technique, which has been described in a previous study⁶. To avoid performing experiments with radioactive I-129, only stable I-127 was used in this study. The as-fabricated pellet was abraded to 1200 grit and then cleaned with ethanol and deionized water (DI) water. NaCl was purchased from Fisher Scientific and used without further purification. All solutions were prepared with DI water with a minimum electrical resistivity of 18 MΩ cm. Prior to the corrosion experiments, perfluoroalkoxy alkane (PFA) containers and PTFE specimens and tape were pretreated with 5 wt% NaOH solution and DI water to remove fluoride ions⁵⁵.

Corrosion experiment

A SS specimen was pressed against an I-APT specimen and corroded in 0.6 M NaCl solution. All specimens were pre-wetted with NaCl solution immediately before immersion. The assembly was wrapped with Teflon tape to secure the specimen positions during the immersion. The experiment was conducted in PFA containers, which were placed in a water bath with temperature adjusted and maintained at 90 ± 0.1 °C, which is a temperature commonly used for accelerated laboratory testing. To prevent crevice corrosion between SS and the containers, the SS specimen was placed on top of the I-APT, while the other side of I-APT was in contact with the PFA container. Control experiments were conducted by pressing I-APT against PTFE specimens and corroding them under similar conditions. After 7 or 28 days, the assemblies were removed from the solution. The specimens were separated and rinsed with abundant DI water and then dried with compressed air.

Optical microscopy and optical profilometry

The corrosion morphology of corroded SS samples was examined by an optical microscope (Olympus PME 3). 3D topography of corroded samples was obtained by an optical profilometry (Bruker Contour GT). Stitching was enabled to achieve the images on the scale of a few millimeters.

Scanning electron microscopy/energy dispersive spectroscopy (SEM/EDS)

The morphological and chemical changes of SS after 28 days of corrosion were further explored by an SEM (Thermo Fisher Scientific Apreo FEG) equipped with an EDAX Octane Elect EDS System (AMETEK). All images were collected with a working distance less than 10 mm. An acceleration voltage of 15.0 kV was used. The beam current was 6.4 nA.

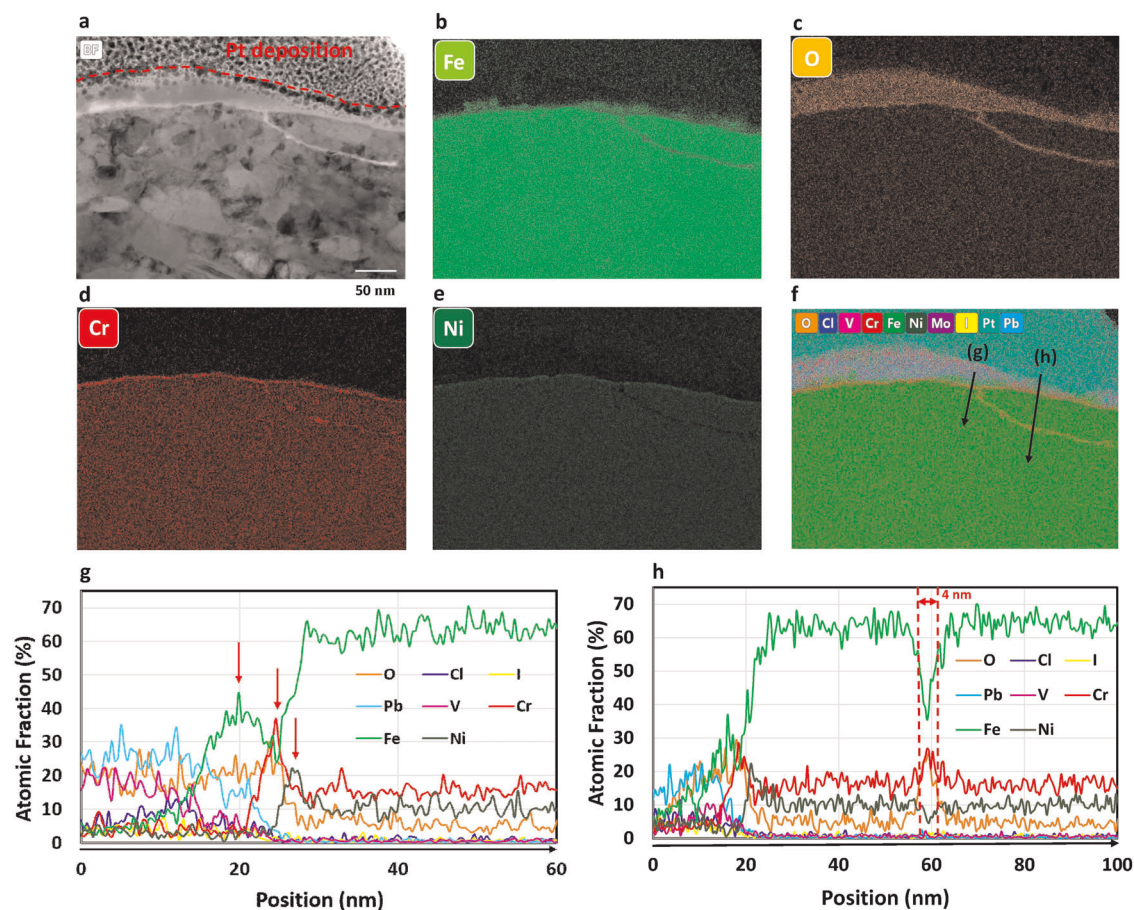


Fig. 10 STEM/EDS characterizations for the cross-section of a sample lifted from an area of SS that was located inside the crevice. **a** A bright-field STEM image showing the existence of a nano-crack on the corroded SS surface. **b–f** Individual EDS elemental mapping for the area shown in **(a)**. **g, h** EDS line scan for two regions as indicated by the black arrows shown in **(f)**.

Raman spectroscopy

The SS specimens corroded for 7 days were analyzed using a Renishaw inVia confocal Raman spectrometer equipped with a 50× objective. A 514 nm laser was used as the exciting beam with power of 12 mW at the sample. Prior to the measurement, the Raman shift was calibrated with a silicon reference. The spectra were acquired from areas with and without precipitates on the SS samples. The areas with precipitates were referred to as Spot 1–3, while the area without precipitates was referred to as matrix (Fig. 3).

X-ray photoelectron spectroscopy (XPS)

The surface chemistry of SS after 28 days of corrosion was analyzed by a Kratos XPS system. Monochromatic Al-Kα electrons (1486.6 eV, 120 W) were used as the X-ray excitation source. The emission current was 10 mA and the bias voltage was 140 V. The filament limit current was 4.9 V. The spectra were collected at 0.1 eV steps and 20 eV pass energy. The area of analysis was approximately 400 μm × 600 μm. The data were analyzed with CasaXPS software. All spectra were calibrated to the adventitious C 1s peak located at 284.8 eV⁵⁶. The concentrations of different species were quantified with the following equation⁵⁷:

$$c_x = \frac{I_x/S_x}{\sum I_i/S_i},$$

where c_x is the concentration of species x in the alloy, I_x is the peak intensity acquired by XPS, and S_x is the corresponding sensitivity factor. C peak area was not included in the calculation of surface compositions.

Scanning/transmission electron microscopy (S/TEM)

TEM samples were lifted out from locations inside and outside the crevice area and carefully prepared using a FEI Quanta 3D field emission gun dual

beam FIB system. To protect the original features, a platinum (Pt) coating was deposited on the corroded SS surface. The deposition was conducted in multiple steps. Firstly, a thin layer of 0.1 μm was achieved by electron beam deposition. This step was followed by ion beam deposition with a gradually increased ion beam current until a thickness of about 3 μm was achieved. The thickness of the lifted TEM samples were gradually reduced to ~100 nm, followed by a final cleaning process (2 kV/27 pA, ~3 min on each side) to remove the Ga ion induced damages. Partial of Pt deposition was preserved at the end of thinning. A 200 kV FEI F200X Talos S/TEM equipped with an EDS system was used for THE microstructure and composition analysis on the prepared TEM foil samples.

DATA AVAILABILITY

The data that support the findings of this study are available from the corresponding author upon request.

Received: 5 February 2020; Accepted: 3 April 2020;
Published online: 12 May 2020

REFERENCES

- Cohen, B. L. High-level radioactive waste from light-water reactors. *Rev. Mod. Phys.* **49**, 1 (1977).
- Sava, D. F., Garino, T. J. & Nenoff, T. M. Iodine confinement into metal–organic frameworks (MOFs): low-temperature sintering glasses to form novel glass composite material (GCM) alternative waste forms. *Ind. Eng. Chem. Res.* **51**, 614–620 (2011).
- Jie, K. et al. Reversible iodine capture by nonporous pillar [6] arene crystals. *J. Am. Chem. Soc.* **139**, 15320–15323 (2017).

4. Ma, S. et al. Highly efficient iodine capture by layered double hydroxides intercalated with polysulfides. *Chem. Mater.* **26**, 7114–7123 (2014).
5. Yao, T. et al. Bulk iodoapatite ceramic densified by spark plasma sintering with exceptional thermal stability. *J. Am. Ceram. Soc.* **97**, 2409–2412 (2014).
6. Yao, T., Scott, S., Xin, G., Lu, F. & Lian, J. Dense iodoapatite ceramics consolidated by low-temperature spark plasma sintering. *J. Am. Ceram. Soc.* **98**, 3733–3739 (2015).
7. Audubert, F., Carpena, J., Lacout, J. & Tetard, F. Elaboration of an iodine-bearing apatite iodine diffusion into a $Pb_3(VO_4)_2$ matrix. *Solid State Ion.* **95**, 113–119 (1997).
8. Sales, B. & Boatner, L. Physical and chemical characteristics of lead-iron phosphate nuclear waste glasses. *J. Noncryst. Solids* **79**, 83–116 (1986).
9. Guo, X. et al. Self-accelerated corrosion of nuclear waste forms at material interfaces. *Nat. Mater.* **19**, 310–316 (2020).
10. Guo, X. et al. Near-field corrosion interactions between glass and corrosion resistant alloys. *npj Mater. Degrad.* <https://doi.org/10.1038/s41529-020-0114-1> (2020).
11. Zhang, Z. et al. Effect of solution chemistry on the iodine release from iodoapatite in aqueous environments. *J. Nucl. Mater.* **525**, 161–170 (2019).
12. Kerrisk, J. F. Groundwater chemistry at Yucca Mountain, Nevada, and vicinity. No. LA-10929-MS. (Los Alamos National Lab., 1987).
13. Hem, J. D. *Study and Interpretation of the Chemical Characteristics of Natural Water* (Department of the Interior, US Geological Survey, 1985).
14. Oldfield, J. & Sutton, W. Crevice corrosion of stainless steels: I. A mathematical model. *Br. Corros. J.* **13**, 13–22 (1978).
15. Kelly, R. G. in *Encyclopedia of Electrochemistry* (ed A. J. Bard) 275–307 (2007).
16. Long, J. C. & Ewing, R. C. Yucca Mountain: earth-science issues at a geologic repository for high-level nuclear waste. *Annu. Rev. Earth Planet. Sci.* **32**, 363–401 (2004).
17. Stenhouse, M., Apted, M. & Zhou, W. *EPRI Review of Geologic Disposal for Used Fuel and High Level Radioactive Waste: Volume III—Review of National Repository Programs*. (Electric Power Research Institute, Palo Alto, CA, 2010).
18. Zhang, M., Maddrell, E., Abratis, P. & Salje, E. Impact of leach on lead vanado-iodoapatite $[Pb_2(VO_4)_3]$: An infrared and Raman spectroscopic study. *Mater. Sci. Eng. B* **137**, 149–155 (2007).
19. Griffith, W. & Lesniak, P. Raman studies on species in aqueous solutions. Part III. Vanadates, molybdates, and tungstates. *J. Chem. Soc. A* 1066–1071 (1969).
20. Mesmer, R. & Baes, C. *The Hydrolysis of Cations* (Wiley, EUA, 1976).
21. Dieterle, M., Weinberg, G. & Mestl, G. Raman spectroscopy of molybdenum oxides Part I. Structural characterization of oxygen defects in MoO_{3-x} by DR UV/VIS, Raman spectroscopy and X-ray diffraction. *Phys. Chem. Chem. Phys.* **4**, 812–821 (2002).
22. Biesinger, M. C. et al. Resolving surface chemical states in XPS analysis of first row transition metals, oxides and hydroxides: Cr, Mn, Fe, Co and Ni. *Appl. Surf. Sci.* **257**, 2717–2730 (2011).
23. Poole, R., Kemény, P., Liesegang, J., Jenkin, J. & Leckey, R. High resolution photoelectron studies of the d bands of some metals. *J. Phys. F: Met. Phys.* **3**, L46 (1973).
24. Choi, J.-G. & Thompson, L. XPS study of as-prepared and reduced molybdenum oxides. *Appl. Surf. Sci.* **93**, 143–149 (1996).
25. McIntyre, N., Johnston, D., Coatsworth, L., Davidson, R. & Brown, J. X-ray photoelectron spectroscopic studies of thin film oxides of cobalt and molybdenum. *Surf. Interface Anal.* **15**, 265–272 (1990).
26. Kawafune, I. & Matsubayashi, G.-e. Isolation and characterization of oxygen-deficient reduced forms of the dodecamolybdophosphate anion salt. *Inorg. Chim. Acta* **188**, 33–39 (1991).
27. Haber, J., Machej, T., Ungier, L. & Ziolkowski, J. ESCA studies of copper oxides and copper molybdates. *J. Solid State Chem.* **25**, 207–218 (1978).
28. Deltombe, E., de Zoubov, N. & Pourbaix, M. in *Atlas of Electrochemical Equilibria in Aqueous Solution 272-279* (Pergamon Press Oxford, 1966).
29. Benoist, L. et al. XPS analysis of lithium intercalation in thin films of molybdenum oxysulphides. *Surf. Interface Anal.* **22**, 206–210 (1994).
30. Anwar, M., Hogarth, C. & Bulpett, R. Effect of substrate temperature and film thickness on the surface structure of some thin amorphous films of MoO_3 studied by X-ray photoelectron spectroscopy (ESCA). *J. Mater. Sci.* **24**, 3087–3090 (1989).
31. Seifert, G., Finster, J. & Müller, H. SW Xa calculations and x-ray photoelectron spectra of molybdenum (II) chloride cluster compounds. *Chem. Phys. Lett.* **75**, 373–377 (1980).
32. Frankel, G. Pitting corrosion of metals a review of the critical factors. *J. Electrochem. Soc.* **145**, 2186–2198 (1998).
33. Nefedov, V., Firsov, M. & Shaplygin, I. Electronic structures of $MRhO_2$, MRh_2O_4 , $RhMO_4$ and Rh_2MO_6 on the basis of X-ray spectroscopy and ESCA data. *J. Electron Spectrosc. Relat. Phenom.* **26**, 65–78 (1982).
34. Nefedov, V., Salyn, Y. V. & Keller, K. X-ray electron studies of lead and mercury-compounds. *Inst. Obs Neorg. Khimii Im. Ns Kurnakova Lenin. Prospekt 31, 71 Moscow, Russia* **24**, 2564–2566 (1979).
35. Nefedov, V., Salyn, Y. V., Solozhenkin, P. & Pulatov, G. Y. X-ray photoelectron study of surface compounds formed during flotation of minerals. *Surf. Interface Anal.* **2**, 170–172 (1980).
36. Sakurada, O., Takahashi, H. & Taga, M. X-ray photoelectron spectroscopic study of the stabilization of lead with a palladium modifier in graphite-furnace AAS. *Bunseki Kagaku* **38**, 407–412 (1989).
37. Zhang, Z. et al. Mechanism of iodine release from iodoapatite in aqueous solution. *RSC Adv.* **8**, 3951–3957 (2018).
38. Schnyder, B. et al. UV-irradiation induced modification of PDMS films investigated by XPS and spectroscopic ellipsometry. *Surf. Sci.* **532**, 1067–1071 (2003).
39. Huang, Y. & Titchmarsh, J. TEM investigation of intergranular stress corrosion cracking for 316 stainless steel in PWR environment. *Acta Mater.* **54**, 635–641 (2006).
40. Stellwag, B. The mechanism of oxide film formation on austenitic stainless steels in high temperature water. *Corros. Sci.* **40**, 337–370 (1998).
41. Marcus, P. On some fundamental factors in the effect of alloying elements on passivation of alloys. *Corros. Sci.* **36**, 2155–2158 (1994).
42. Iannuzzi, M. & Frankel, G. S. Mechanisms of corrosion inhibition of AA2024-T3 by vanadates. *Corros. Sci.* **49**, 2371–2391 (2007).
43. Ralston, K. D., Chrisanti, S., Young, T. L. & Buchheit, R. G. Corrosion inhibition of aluminum alloy 2024-T3 by aqueous vanadium species. *J. Electrochem. Soc.* **155**, C350–C359 (2008).
44. Iannuzzi, M., Kovac, J. & Frankel, G. S. A study of the mechanisms of corrosion inhibition of AA2024-T3 by vanadates using the split cell technique. *Electrochim. Acta* **52**, 4032–4042 (2007).
45. Guo, X., Hurley, B. & Buchheit, R. G. Encapsulation of $NaVO_3$ as corrosion inhibitor into microparticles and its active corrosion protection for AA2024 based upon inhibitor control release. *Corrosion* **71**, 1411–1413 (2015).
46. Anderko, A., Sridhar, N., Jakab, M. & Tormoen, G. A general model for the repassivation potential as a function of multiple aqueous species. 2. Effect of oxyanions on localized corrosion of Fe–Ni–Cr–Mo–W–N alloys. *Corros. Sci.* **50**, 3629–3647 (2008).
47. Morks, M. F., Corrigan, P. A. & Cole, I. S. Mn–Mg based zinc phosphate and vanadate for corrosion inhibition of steel pipelines transport of CO_2 rich fluids. *Int. J. Greenh. Gas Control* **7**, 218–224 (2012).
48. Sribharathy, V. G. & Rajendran, S. Corrosion inhibition of carbon steel by sodium metavanadate. *J. Electrochem. Sci. Eng.* **2**, 121–131 (2012).
49. Zou, Z., Li, N., Li, D., Liu, H. & Mu, S. A vanadium-based conversion coating as chromate replacement for electrogalvanized steel substrates. *J. Alloy. Compd.* **509**, 503–507 (2011).
50. Gao, Z., Zhang, D., Jiang, S., Zhang, Q. & Li, X. XPS investigations on the corrosion mechanism of V (IV) conversion coatings on hot-dip galvanized steel. *Corros. Sci.* **139**, 163–171 (2018).
51. Shropshire, J. A. Inhibition of acid attack on steel by heavy metal ions. *J. Electrochem. Soc.* **107**, 740–744 (1960).
52. Mayne, J. & Turgoose, S. Inhibition of the corrosion of iron by lead azelate: I. Uptake and distribution of azelate and lead ions. *Br. Corros. J.* **11**, 204–207 (1976).
53. Lafranconi, G., Mazza, F., Sivieri, E. & Torchio, S. The inhibiting action of Pb^{2+} on stress corrosion cracking of austenitic stainless steels in acidic chloride media. *Corros. Sci.* **18**, 617–629 (1978).
54. Ateya, B. & Pickering, H. On the nature of electrochemical reactions at a crack tip during hydrogen charging of a metal. *J. Electrochem. Soc.* **122**, 1018–1026 (1975).
55. Jantzen, C. M. & Bibler, N. E. The Product Consistency Test (ASTM C1285) for Waste Form Durability Testing. in *Environmental Issues and Waste Management Technologies in the Ceramic and Nuclear Industries XI: Proceedings of the 107th Annual Meeting of The American Ceramic Society, Baltimore, Maryland, USA, Ceramic Transactions. 141* (Wiley-American Ceramic Society, 2005).
56. Guo, X., Hurley, B., Yang, F. & Buchheit, R. A novel organic conversion coating based on N-benzoyl-N-phenylhydroxylamine chemistry for the corrosion protection of AA2024-T3. *Electrochim. Acta* **246**, 197–207 (2017).
57. Moulder, J. F. *Handbook of X-ray photoelectron spectroscopy. Phys. Electron* **24**, 25 (1995).

ACKNOWLEDGEMENTS

This work was supported as part of the Center for Performance and Design of Nuclear Waste Forms and Containers, an Energy Frontier Research Center funded by the U.S. Department of Energy, Office of Science, Basic Energy Sciences under Award # DESC0016584. The authors would like to thank Yutichai Mueangngern and Dr. Yehia Khalifa from Ohio State University for their assistance with XPS measurement.

AUTHOR CONTRIBUTIONS

X.G. and Y.W. contributed equally to this work. X.G. conceived the idea; X.G., Y.W., T.Y., C.M. conducted the experiments and analyzed the data; J.L. and G.S.F. supervised the study. All authors contributed to the editing of the paper, and approval of the content in its current form.

COMPETING INTERESTS

The authors declare no competing interests.

ADDITIONAL INFORMATION

Correspondence and requests for materials should be addressed to X.G.

Reprints and permission information is available at <http://www.nature.com/reprints>

Publisher's note Springer Nature remains neutral with regard to jurisdictional claims in published maps and institutional affiliations.



Open Access This article is licensed under a Creative Commons Attribution 4.0 International License, which permits use, sharing, adaptation, distribution and reproduction in any medium or format, as long as you give appropriate credit to the original author(s) and the source, provide a link to the Creative Commons license, and indicate if changes were made. The images or other third party material in this article are included in the article's Creative Commons license, unless indicated otherwise in a credit line to the material. If material is not included in the article's Creative Commons license and your intended use is not permitted by statutory regulation or exceeds the permitted use, you will need to obtain permission directly from the copyright holder. To view a copy of this license, visit <http://creativecommons.org/licenses/by/4.0/>.

© The Author(s) 2020